Journal of Materials Chemistry C

ROYAL SOCIETY OF CHEMISTRY

PAPER

View Article Online
View Journal | View Issue

Cite this: J. Mater. Chem. C, 2021, 9, 4351

Lead-free zero dimensional tellurium(IV) chloride-organic hybrid with strong room temperature emission as a luminescent material†

Anupam Biswas,[ab] Rangarajan Bakthavatsalam,[ab] Vir Bahadur,[ab] Chinmoy Biswas,[c] Bhupendra P. Mali,[ab] Sai Santosh Kumar Raavi,[c] Rajesh G. Gonnade[ab] and Janardan Kundu *[d]

Received 7th December 2020,
Accepted 15th February 2021

DOI: 10.1039/d0tc05752e

rsc.li/materials-c

Despite the current progress in 'Pb-free' low dimensional main group metal halide based luminescent materials, it is challenging to synthesize Te(IV) halide hybrids with strong ambient emission with excitation features in the visible range as efficient and stable phosphors for potential lighting applications. Reported here is a (benzyltriethylammonium)$_2$TeCl$_6$ zero dimensional hybrid material with excitation features in the visible range and strong room temperature, broadband, intrinsic luminescence (PLQY ~15%) arising due to self-trapped excitons (STEs). Furthermore, a proof-of-concept LED architecture demonstrates successful optical down-conversion with a visible light excitation source. Here, exclusive adoption of a 'regular' octahedral Te(IV)-halide unit structure with minimal static distortion provides a unique opportunity to unmask the role played by 5s^2 lone pair electrons in shaping the emissive properties. This effort may open up new avenues towards unravelling the role of lone pair stereoactivity in controlling the PLQY in low dimensional hybrids that has proven to be challenging for the reported (Sb, Sn) based low dimensional 5s^2 metal halide hybrid materials.

Introduction

Metal halide-organic hybrid perovskites with fascinating properties have been at the research forefront of energy related applications such as solar cells, LEDs, lasers, and photodetectors.[1–3] For 3D perovskites, featuring three dimensional networked metal halide units, the photo-generated excitons are weakly bound and can diffuse in all directions within the inorganic framework with long diffusion lengths (~1 μm).[4] Organic ligand size induced dimensionality lowering (2D, 1D, 0D) restricts the exciton due to quantum and dielectric confinement with high exciton binding energies.[5] Typically, in 0D perovskites, the metal halide unit (square pyramidal, octahedral, disphenoidal) is isolated and surrounded by bulky organic ligands supporting strongly bound excitons that can relax radiatively across the band edge.[6–8] Lowered dimensionality in these materials further allows trapping of the generated excitons into the lattice sites through transient structural distortion. Such self-trapping of excitons[9] is facilitated due to the soft nature of the material and strong electron–phonon coupling.[10] Recombination of these self-trapped excitons (STE) leads to a broad emission band with generally longer lifetimes.[9,11,12] The involvement of lattice phonon modes further broadens the emission profile with an accompanying excitation energy dissipation (Stokes shift) due to the significant excited state structural reorganization.[13] These factors cumulatively lead to a strong, Stokes shifted, broad band emission profile in low dimensional hybrid perovskites.[14] Moreover, the presence of the inorganic unit embedded within the organic ligand matrix endows environmental stability. These enabling properties have encouraged their applications in light emitting devices, solar concentrators, and radiation detectors.[14]

Many low dimensional Pb(II)-halides (6s^2 lone pair) have been reported to show STE based broadband white light emission properties.[15] The broadband emission intensity has been correlated to the structural distortions (out of plane, in plane deformations) for the 2D Pb hybrids.[15] However, no such correlation is observed to hold for 1D/0D based Pb hybrids. Nevertheless, the recent search for 'Pb free' variants has

[a] CSIR-National Chemical Laboratory, Pune, India
[b] Academy of Scientific and Innovative Research (AcSIR), Ghaziabad, India
[c] Indian Institute of Technology Hyderabad, Kandi, India
[d] Indian Institute of Science Education and Research (IISER) Tirupati, Tirupati, India. E-mail: janardan@iisertirupati.ac.in

† Electronic supplementary information (ESI) available: Single crystal structure experimental details, XPS, NMR, Tauc Plot, optical characterization, lifetime decay profiles, structural distortion parameters, single crystal data with various bond angles and bond lengths, grinding and annealing photophysical characterization, Raman spectra, fitting of low temperature PL data, configuration coordinate diagram, TGA data, and stability data. CCDC 2042525. For ESI and crystallographic data in CIF or other electronic format see DOI: 10.1039/d0tc05752e

kindled immense research interest in main-group metal halides with $5s^2$ lone pairs (*viz.* Sn^{2+}, Sb^{3+}).[16] Antimony(III) halide-organic 0D hybrids featuring oxidative stability, $5s^2$ electronic configuration, and isolated metal-halide units (octahedral, square pyramidal, disphenoidal, *etc.*), have been demonstrated to support efficient broadband emission with high photoluminescence quantum yield (PLQY).[6,7,17–21] The broad band emission in such Sb(III) halide systems has been fully attributed to the radiative recombination of STEs originating from the excited triplet state of the Sb^{3+} centre ($^3P_1$) with typically longer emission lifetimes (3–10 μs).[14,21] There is no experimental evidence of a correlation between the structural distortions and PLQY for the 0D Sb hybrids. $5s^2$ lone pair activity induced structure and distortion of the metal halide unit (static and/or dynamic), is believed to affect the luminescence properties in Sb(III) halide systems.[14,22] However, formulating a rational design strategy aimed to unmask the role played by the Sb^{3+} $5s^2$ lone pair in shaping their luminescence properties has turned out to be challenging due to the adopted variety of isolated metal-halide unit structures (octahedral, square-pyramidal, disphenoidal). Moreover, the majority of these Sb based 0D materials lack excitation features in the visible range and necessitates them to be paired with UV LEDs (that are currently expensive and inefficient) for their application as down-conversion phosphors.[14]

Tellurium(IV), featuring a $5s^2$ lone pair, also forms zero dimensional hybrids with a metal halide semiconducting unit dispersed in the organic ligand matrix.[23] The high charge density on the Te^{4+} centre supports a greater number of halide ligands and exclusively generates octahedral units irrespective of the counter organic cation.[24–26] The most commonly adopted structure is vacancy ordered double perovskite (A_2TeX_6)[24,27] with almost 'regular' octahedral coordination. Given this structural simplicity (compared to Sb^{3+}), high oxidative stability, and $5s^2$ configuration (similar to Sb^{3+}) for the Te(IV) halides, it is expected that low dimensional Te(IV) halides would demonstrate exceptional luminescence properties. The exclusive adoption of octahedral metal-halide geometry in $[TeX_6]^{2-}$ systems (unlike Sb^{3+} systems) would allow the formulation of a design strategy to draw any structure/distortion - PLQY correlation. Encouragingly, there have been studies on $[TeX_6]^{2-}$ hybrids that report structural[28–32] and photo-physical properties[25,26,33] presenting excitation features in the visible range. Unfortunately, these $[TeX_6]^{2-}$ hybrids have not been demonstrated to be strongly emissive at room temperature as the quenching temperatures are relatively low in these compounds[34] and those that do emit at room temperature are very weak with low PLQYs.[25,26,33]

It is clear that enhancing the room temperature PLQY of $[TeX_6]^{2-}$ hybrids is of huge importance in deciphering the structure/distortion-property correlation that is currently absent for 0D metal halide hybrids (Pb, Sb, Sn). In this first effort, we demonstrate a tellurium(IV) chloride based zero dimensional hybrid featuring isolated, undistorted $[TeCl_6]^{2-}$ octahedral units embedded in the organic templating ligand (benzyltriethylammonium: BzTEA) matrix that show intrinsic, broad, yellow-orange, strong room temperature emission (PLQY ~15%) with ambient/thermal stability, and excitation feature in the visible range (445 nm) allowing for their use as potential down-conversion phosphor materials. The synthesized $(BzTEA)_2TeCl_6$ product shows long lived and broad band emission likely due to self-trapping of excitons (STEs). The emissive characteristics are observed to be independent of the particle size, surface, and other structural defects and hence the utilized synthetic route. This supports the unique and intrinsic nature of the STE based emission. This tellurium(IV) halide hybrid with room temperature emission and excitation band in the visible range could serve as a potential 'Pb-free' stable phosphor material for lighting applications as demonstrated here with a test-bed down-conversion LED architecture. Noteworthily, ambient emitting octahedral (exclusive geometry) $[TeX_6]^{2-}$ hybrids could further be leveraged to gain a rational understanding of the structure/distortion – photophysical property correlation.

Experimental section

Materials

Tellurium tetrachloride (99.99%), hydrochloric acid (37%), acetone, and dimethylformamide were purchased from Sigma Aldrich. Benzyltriethylammonium chloride (98%) was purchased from TCI Chemicals. Diethyl ether was purchased for HiMedia. All chemicals were used as purchased without further purification.

Synthesis of $(BzTEA)_2TeCl_6$ crystals

For the preparation of $(BzTEA)_2TeCl_6$ crystals, 0.1 mmol (26.9 mg) of tellurium tetrachloride was dissolved in 1 mL of dimethylformamide. To this, 0.1 mmol (22.7 mg) benzyltriethylammonium chloride salt was added and dissolved. The resultant solution was used for crystallization with an anti-solvent diffusion method using diethyl ether. The resulting yellow coloured crystals were filtered and washed with acetone repeatedly and dried under vacuum for further characterization. The same crystals can also be prepared using the HX method wherein hydrochloric acid is used as a solvent. For typical HX synthesis, 0.1 mmol (26.9 mg) of tellurium tetrachloride and 0.1 mmol (22.7 mg) benzyltriethylammonium chloride amine were dissolved in hydrochloric acid followed by heating to get a clear yellow solution followed by natural cooling to get the crystals. The crystals of the ground powders were used for further characterization.

Methods

UV-Vis absorbance was performed in a Shimadzu UV-VIS-NIR3600Plus spectrometer. Steady State PL and lifetime were measured using an Edinburgh FS5 spectrophotometer. TGA measurements were performed using a TAG system (Mettler-Toledo, Model TGA/SDTA851e) and samples were heated in the range of 25–800 °C at a heating rate of 5 °C min^{-1} under a nitrogen atmosphere. Absolute quantum yield measurements were carried out in a Horiba JOBIN YVON Fluoromax-4 spectrometer with a calibrated integrating sphere attachment. X-ray photoelectron spectroscopy (XPS) characterization was performed with an ESCALab spectrometer having an Al Kα X-ray source

($h\upsilon$ = 1486.6 eV) operating at 150 W using a Physical Electronics 04-548 dual Mg/Al anode and in a UHV system with a base pressure of $\leq 5 \times 10^{-9}$ Torr. Low temperature PL of the crystals was performed using an Edinburgh FLS1000 photoluminescence spectrometer, attached with an OptistatDN cryostat and the temperature was controlled using a Mercury iTC temperature controller (Oxford instruments). The sample was excited using a xenon lamp and emission was collected from 320 nm to 800 nm. Single crystal X-ray intensity data measurements of crystals were carried out on a Bruker D8 VENTURE Kappa Duo PHOTON II CPAD diffractometer. The intensity measurements were carried out with a Mo microfocus sealed tube diffraction source (Mo Kα = 0.71073 Å) at 100(2) K. The powder X-ray diffraction measurements were carried out on a Rigaku Micromax-007HF instrument (high intensity microfocus rotating anode X-ray generator) with *R*-axis detector IV++ with a scanning rate of 2° 2θ min^{-1} using Cu and Mo Kα radiation. The PXRD sample was prepared by sealing 2–3 mg of finely ground powder into a Lindeman glass capillary with an inner diameter of 1 mm. Raman spectroscopic measurements were recorded at room temperature on an HR 800 Raman spectrophotometer (Jobin Yvon, Horiba, France) using monochromatic radiation (achromatic Czerny–Turner type monochromator with silver treated mirrors) emitted by a He–Ne laser (633 nm). For down-conversion LED measurements a commercially available blue LED (λ_{emi} = 447 nm, FWHM = 20 nm) was used. The $(BzTEA)_2TeCl_6$ crystal was ground and coated on the flat surface of the commercially available blue LED for spectroscopic analysis and imaging. Furthermore, the spectroscopic details were measured using an Edinburgh FS5 spectrophotometer and images were captured by using a digital camera (Canon PowerShot SX740 HS).

Results and discussion

$(BzTEA)_2TeCl_6$ single crystals were synthesized by the anti-solvent diffusion method (Fig. 1a). Yellow colored single crystals of $(BzTEA)_2TeCl_6$ formed within a day that emitted an intense yellow-orange light under UV illumination (Fig. 1a and b). XPS analysis confirms the presence of Te^{4+} and Cl^- ions in the product (Fig. S1, ESI†). ^{1}H NMR analysis confirms the presence of a cationic ligand moiety (Fig. S2, ESI†).

Optical absorption characterization of the crystals (Fig. 2a) shows a sharply rising absorption edge (absorption onset ~515 nm) with absorption bands at 440 nm, 380 nm, 295 nm, and 270 nm. These absorption bands originate due to the transitions between the sp excited state and the s^2 ground state of the Te(IV) centre: $^1S_0 \rightarrow {}^3P_1$, $^3P_2$, and $^1P_1$ (free ion term symbols) and possibly due to ligand to metal charge transfer absorption at shorter wavelengths.[13] Direct band gap Tauc plot analysis estimates an optical band gap of ~2.57 eV (Fig. S3, ESI†). Room temperature steady state photoluminescence (PL) characterization of the crystals (Fig. 2a) shows broad band (full width at half maximum: FWHM = 130 nm) emission with a strong PL peak (λ_{emi} = 608 nm; λ_{exc} = 440 nm).

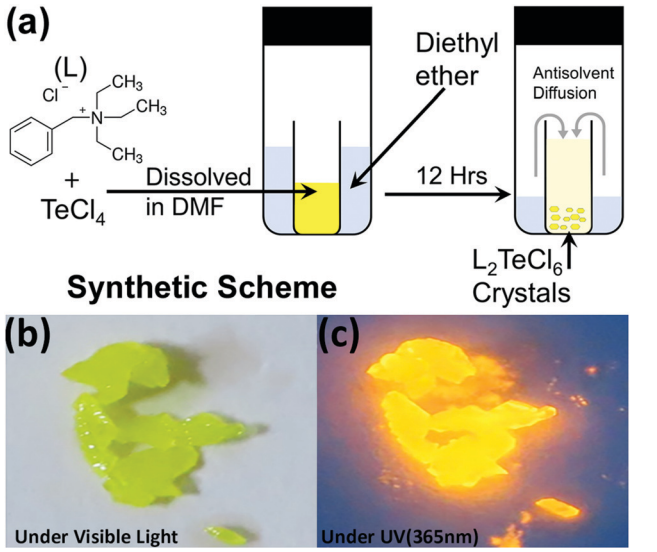

Fig. 1 (a) Reaction scheme (anti-solvent diffusion) utilized for the synthesis of single crystals of $(BzTEA)_2TeCl_6$; photograph of the synthesized crystals at room temperature under (b) visible and (c) UV illumination (365 nm).

The photoluminescence excitation (PLE) spectrum of the crystals (λ_{emi} = 600 nm) shows features in the 300–500 nm range with a strong excitation band at 445 nm. The observed features and onset of PLE match well with the absorption spectra. The estimated Stokes shift is ~160 nm that minimizes self-reabsorption losses. The room temperature photoluminescence quantum yield (PLQY) is estimated to be 15% attesting to the observed strong visible ambient emission. Time resolved PL measurements (μs flash lamp source) across the broad band (decay profiles: Fig. 2b, extracted lifetimes, and relative weights Fig. S4, ESI†) of the crystals demonstrates long lifetime components [~1.1 μs (44%), ~9.9 μs (56%)] in line with the exciton recombination mechanism originating from the lowest triplet state ($^3P_1 \rightarrow {}^1S_0$, forbidden transition). The strong spin–orbit coupling and high Te–Cl bond covalency (~80%) can allow for appreciable relaxation of the spin forbiddances leading to strong luminescence as observed here. Furthermore, the generality of the utilized reaction procedure (solvent-antisolvent, HX) for the synthesis of Te(IV) based low dimensional perovskites are demonstrated here for two other ligands [tetraethylammonium chloride, tris(2-aminoethyl)amine in HCl] and their optical characterization is summarized in Fig. S5, ESI.† Noteworthily, these products have very weak ambient emission when directly compared to that of the $(BzTEA)_2TeCl_6$ hybrid (Fig. S6, ESI†).

The overview of the single crystal structure of the $(BzTEA)_2TeCl_6$ product (CCDC 2042525†) is shown in Fig. 3. The product crystallized in the monoclinic $P2_1/n$ space group containing one organic ligand ($[C_{13}H_{22}N]^+$) and $\frac{1}{2}$ unit of $[TeCl_6]^{2-}$ octahedron in the asymmetric unit (Fig. 3b) leading to the molecular formula of $[C_{13}H_{22}N]_2TeCl_6$. The product has an isolated metal halide octahedron periodically dispersed in the organic ligand matrix generating a zero dimensional vacancy-ordered double perovskite structure (Fig. 3a). The inorganic unit features a nearly 'regular' metal halide octahedron with minimal distortions

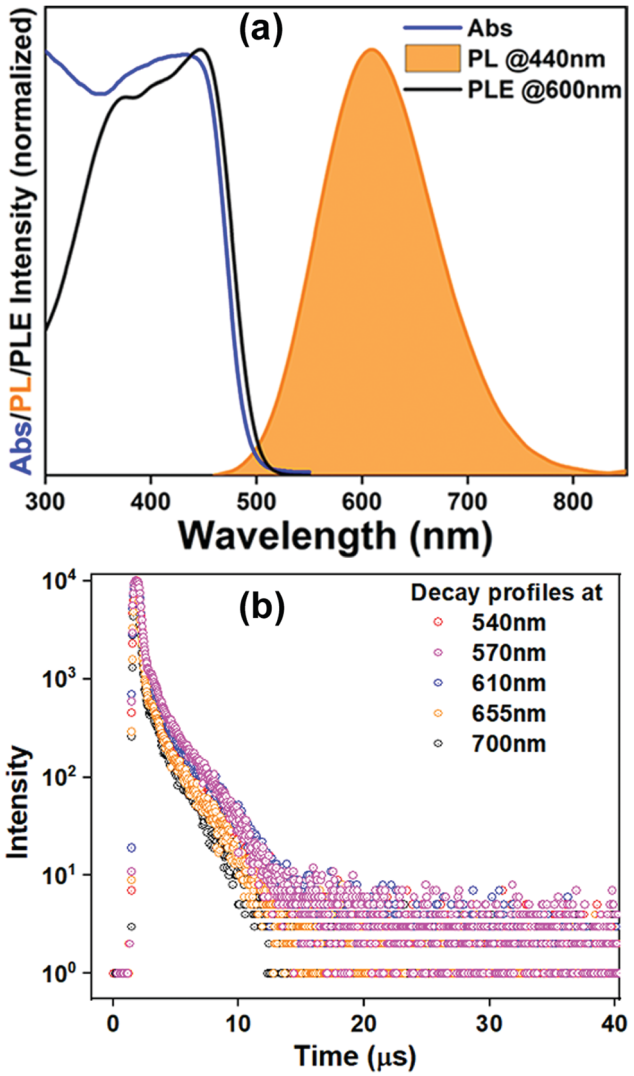

Fig. 2 Optical characterization of $(BzTEA)_2TeCl_6$ showing (a) absorbance (Abs), photoluminescence (PL), and photoluminescence excitation (PLE) spectra; (b) lifetime decay profiles collected across the PL band (λ_{exc} = 440 nm).

(largest difference in Te–Cl bond length = 0.025 Å; Fig. 3c; largest deviation of the Cl–Te–Cl bond angle from ideal value = 0.9°; Fig. S7, ESI†) with quadratic elongation of 1.0001 and bond angle variance of 0.33 $(degree)^2$ attesting to the low stereochemical activity of the $5s^2$ lone pair. High charge on the metal centre, supporting six coordination, reduces the static expression of the lone pair leading to a symmetric metal halide octahedral framework. This near-regularity of the metal halide unit leads to the observation of one broad, featureless, triplet dominated ($^3P_{0,1,2}$) emission peak.[13,14] The phase purity of the product was confirmed using the powder X-ray diffraction pattern that matches well with the simulated one (Fig. 3d).

Given the broad nature of the observed PL emission peak of $(BzTEA)_2TeCl_6$ crystals, it is important to decipher if the broadened emission is due to defect emission. The PL emission profile remains unchanged across a broad excitation range of 320–380 nm (Fig. S8a, ESI†). PLE spectra collected across the broad emission band (Fig. S8b, ESI†) also remain unaltered. Furthermore, the estimated lifetime components across the broad emission band were found to remain unchanged (Fig. S4, ESI†). These observations suggest that unique emissive species are responsible for the broad emission and very likely do not involve extrinsic defects. Furthermore, PL/PLE studies were performed on ground powder samples. If defects led to broad band emission, sample grinding would cause a substantial change of the PL/PLE profile. However, no changes in the PL/PLE band profile were observed when the samples were ground (Fig. S9, ESI†). Moreover, the nature of the PL/PLE profile remains unchanged for the ground crystals when PL is collected at different excitations and PLE is collected across the broad emission band (Fig. S10, ESI†). In addition, the lifetimes of the ground sample across the broad emission band remain almost unchanged (Fig. S11, ESI†). Also, the crystal samples, when annealed at different temperatures, show no changes in the PL/PLE band profile (Fig. S12, ESI†). These observations clearly suggest that the broad emission is not due to the presence of the defects and is due to the presence of unique emissive species that lead to intrinsic emission.

The broad band emissions in low dimensional ns^2 metal halide hybrid materials have been attributed to self-trapping of excitons due to strong electron–phonon coupling that produces transiently localized charges (holes/electrons) that distort the metal halide unit.[14] The PL emission from these STEs is phonon assisted that broadens the radiative bandwidth.[10] Upon photoexcitation, the low lying transient STE states can accept carriers from the excited $^3P_1$ state and allow slow and phonon assisted radiative decay to the $^1S_0$ ground state thereby broadening the emission bandwidth. Concomitantly, the carriers can undergo thermally activated non-radiative recombination that suppresses emission with a strong temperature dependence (thermal quenching of PL due to curve crossing of the excited and ground state[14]). Importantly, excited state reorganization in the $^3P_1$ state and the low lying STE states together dictates the observed Stokes shift in the broad PL emission band.

Low temperature PL measurements were carried out to gain insight into the phonon assisted radiative recombination of STEs leading to the broad band emission. Photoluminescence spectra, collected over the temperature range of 300–80 K (Fig. 4a), show a gradual increase of the PL intensity and band narrowing as the temperature is lowered. Such changes have been generally observed for ns^2 metal halide based 0D materials.[35,36] Integrated PL peak area and FWHM at different temperatures are presented in Fig. 4b. Observed strong PL intensity across the temperature range suggests a low activation energy downhill process of populating the low lying STE states from the $^3P_1$ excited state. The decrease of the PL intensity with increase in temperature further suggests that the STE states have a high self-trapping depth that allows thermally assisted de-trapping followed by fast non radiative recombination only at higher temperatures (Fig. S13, ESI†).[8,15,36] The bandwidth (FWHM) of the broad emission is observed to decrease monotonically as the temperature is lowered as fewer phonon modes are thermally accessible to couple to the STEs assisting radiative recombination.

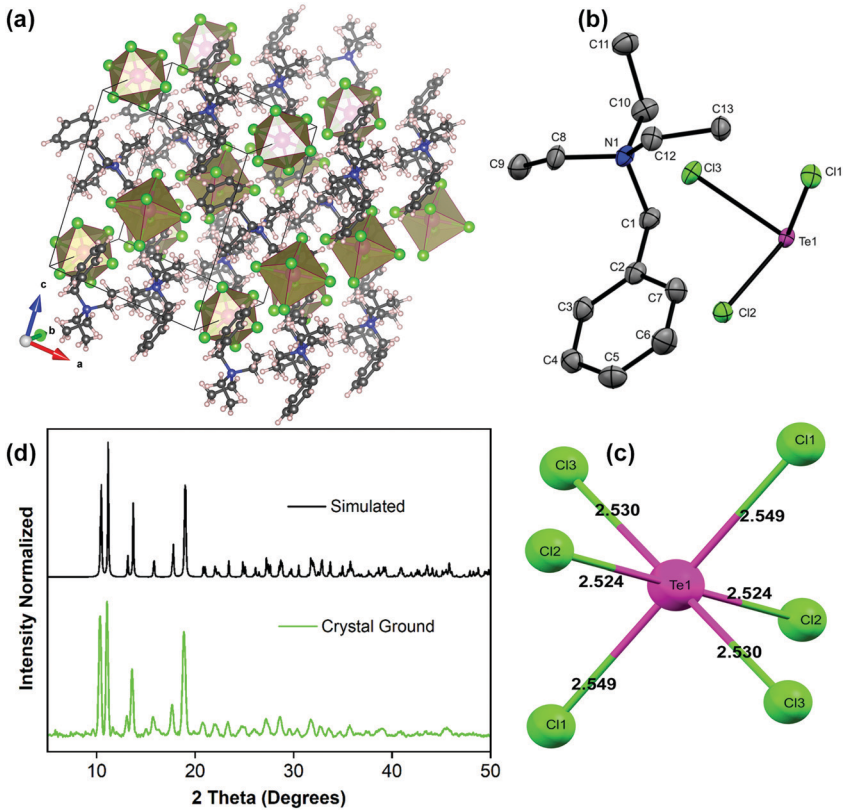

Fig. 3 XRD characterization of the $(BzTEA)_2TeCl_6$ hybrid. Overview of the single crystal structure (a); asymmetric unit (b); site symmetry of Metal-Halide octahedron (c); comparison of the simulated and experimental PXRD pattern using Cu source (d). H atoms are omitted in (b) for clarity.

This temperature dependence of FWHM (Γ) can be fitted to the following equation relating coupling of electronic excitations with the longitudinal optical lattice phonons:[37]

$$\Gamma(T) = \Gamma_0 + \Gamma_{\text{Phonon}}\left(e^{(E_{LO}/k_B T)} - 1\right)^{-1} + \Gamma_{\text{inhomo}} e^{-E_b/k_B T}$$

where, Γ_0 = FWHM at T = 0 K, Γ_{phonon} represents electron–phonon coupling and E_{LO} represents the energy of longitudinal optical phonon mode, Γ_{inhomo} represents inhomogeneous broadening while E_b is the binding energy of trapped states. The fitting and its associated parameters (Fig. S13, ESI†) reflects strong electron–phonon coupling with E_{L_0} = 306 cm^{-1}, in agreement with the low frequency Raman stretching mode of the Te–Cl bond[38,39] of the inorganic metal halide framework (Fig. S14, ESI†). The presence of strong Te–Cl stretching Raman peaks indicates highly polarised phonon modes arising due to strong electron–phonon coupling. The strength of electron–phonon coupling, as quantified in terms of the Huang–Rhys parameter (S), is estimated to be 12.45 (Fig. S15, ESI†). Such a high coupling constant is in close agreement with the reported electron–phonon coupling constants for 0D Sb(III) halide based hybrids.[19] Time resolved PL measurements of the crystals at low temperatures (decay profiles, extracted lifetimes, and relative weights as in Fig. S16, ESI†) show progressive lengthening of the lifetime as the temperature is lowered.

With these observations in mind, the observed photophysical properties can be rationalized in terms of a qualitative configurational coordinate diagram (Fig. 5a) involving the ground state ($^1S_0$), excited states ($^1P_1$, $^3P_{0,1,2}$) and low lying self-trapped states (STEs). Following photon absorption, an electron is promoted to an excited state and, after its thermalization, is trapped in a long-lived STE state. This trapping is then followed by a slow radiative recombination with broadband emission wherein the Stokes shift likely arises due to the excited state structural reorganization. A thermally activated (phonon assisted) de-trapping pathway, followed by a fast non-radiative recombination process (thermal quenching due to intersection of ground and STE states), is also present and competes effectively with the radiative broad band emission at high temperatures. Clearly, the observed strong intrinsic broad band emission at room temperature (and increase of PL intensity with decreasing temperature) is due to efficient STE radiative recombination that dominates over the non-radiative, high activation energy (Fig. S13, ESI†), thermal quenching pathway.

$(BzTEA)_2TeCl_6$ crystals exhibit thermal/ambient stability. Thermogravimetric analysis (TGA) of the product (Fig. S17, ESI†) demonstrates thermal stability up to 160 °C with ligand loss feature at ~200 °C and metal halide unit loss at ~500 °C. The product is stable under ambient conditions over a month with strong persistent photoluminescence (Fig. S18, ESI†) and no discernible changes in the PXRD pattern (Fig. S19, ESI†). To highlight the utility of excitation features in the visible range, a proof-of-concept down-conversion LED was fabricated using a commercially available blue LED (λ_{emi} = 447 nm,

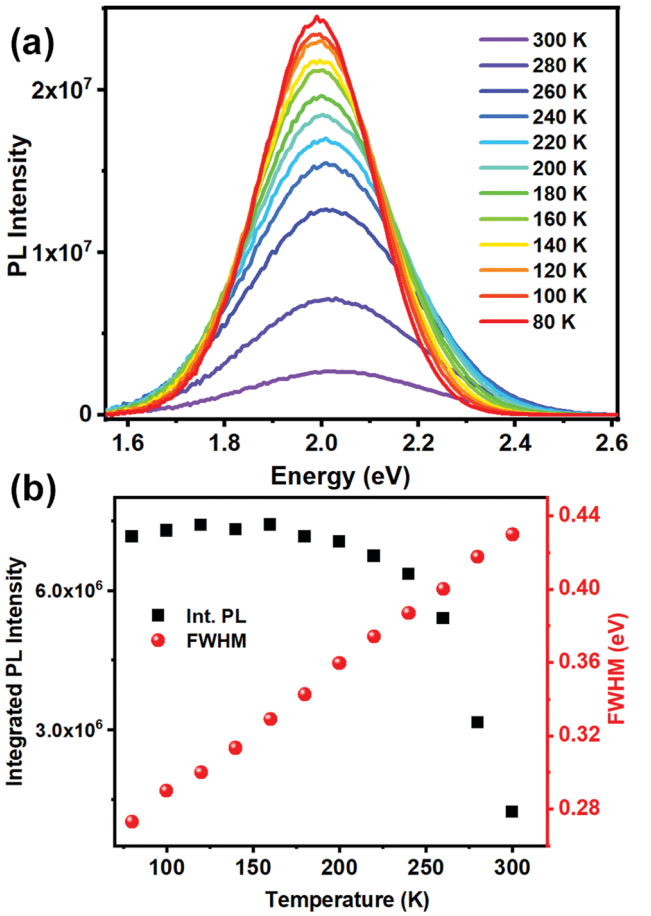

Fig. 4 (a) Low temperature PL (λ_{exc} = 440 nm) spectra of $(BzTEA)_2TeCl_6$ crystals; (b) integrated PL intensity and bandwidth (FWHM) as a function of temperature.

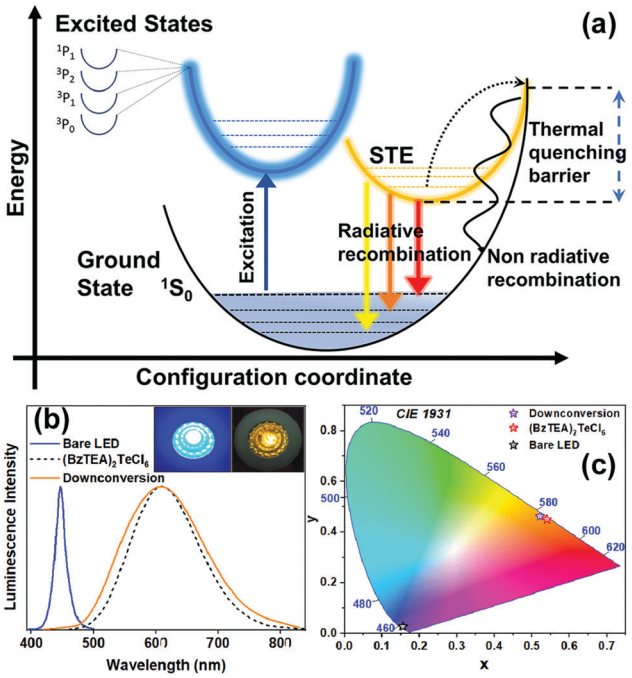

Fig. 5 (a) Schematic representation of the configurational coordinate diagram showing the STE based broad band emission and thermally activated (phonon assisted) non-radiative recombination leading to thermal PL quenching in 0D hybrids. LED characterization (b) electroluminescence of the commercial bare LED, down-converted luminescence from the sample coated LED, and neat sample photoluminescence; inset shows photographs of (i) commercial bare LED and (ii) sample coated down-conversion LED; (c) CIE 1931 Chromaticity coordinate plot for the commercial blue LED, down-conversion LED, and neat sample emission.

FWHM = 20 nm) as the optical source and $(BzTEA)_2TeCl_6$ hybrid as the phosphor material coated on top of the blue LED (Fig. 5b, insets). Electrical biasing of the resultant LED architecture down-converts blue source light to yellow-orange phosphor light characteristic of the $(BzTEA)_2TeCl_6$ hybrid (Fig. 5b). The perceived color of the light emanating from the $(BzTEA)_2TeCl_6$ hybrid, bare LED, and down-conversion LED architecture is presented in the CIE 1931 chromaticity coordinate plot (Fig. 5c) showing successful optical down-conversion using a visible commercial LED. This, by no means, undermines the mild toxicity and rarity of elemental tellurium for their practical applications.

The relevance of the current work within the premise of the burgeoning research efforts on a variety of 0D hybrids (Pb, Sn, Sb) is noted here. Synthesis of strongly emissive (at times near unity PLQY) 0D metal halide hybrids (Sb^{3+}, Pb^{2+}, Sn^{2+}), utilizing organic counter-cationic ligands, relies on a 'hit-or-miss' approach on the choice of ligand. Furthermore, efforts on drawing any correlation between structure/distortion and PLQY for these emissive 0D hybrids (Sb, Sn) (Table S1 and S2, ESI†) have met with limited success due to the adoption of a variety of metal halide coordination geometries (octahedral, square pyramidal, disphenoidal, *etc.*) particularly for Sb^{3+} 0D hybrids. This has deterred designing chemical control on PLQY for these 0D hybrids (Sb, Sn). Interestingly, Te(IV)halide hybrids, that exclusively adopt an octahedral geometry irrespective of the counter cationic ligand, alleviates the above cited drawback faced by Sb(III) hybrids. Hence, $[TeX_6]^{2-}$ hybrids are an apt choice for further investigation of structure/distortion-PLQY correlation studies. However, $[TeX_6]^{2-}$ hybrids typically have low PLQYs at room temperature. Encouragingly, this work demonstrates a $[TeX_6]^{2-}$ hybrid with high room temperature PLQY (~15%). By no means is the achieved PLQY for this $[TeX_6]^{2-}$ hybrid comparable to that of Sb/Sn based hybrids. However, the exclusivity of coordination geometry with modest ambient PLQY of the $[TeX_6]^{2-}$ hybrid opens up the possibility of deciphering structure/distortion – PLQY correlation that is currently missing for the reported main group metal halide (Pb, Sb, Sn) 0D hybrids. Further work on enhancing the ambient PLQY and drawing structure–property correlation for $[TeX_6]^{2-}$ based 0D hybrids is of enormous importance and is currently underway.

Conclusions

In conclusion, we have successfully synthesized $(BzTEA)_2TeCl_6$ zero dimensional vacancy ordered double perovskite with strong room temperature luminescence featuring octahedral

Te(IV) chloride as the inorganic unit embedded in the organic ligand (benzyltriethylammonium chloride) matrix. The product shows long lived, intrinsic self-trapping induced broad band, yellow-orange photoluminescence (λ_{emi} = 610 nm) with high PLQY (15% at room temperature), good thermal/ambient stability, and excitation feature in the visible region ($\sim$445 nm). A test-bed down-conversion LED, fabricated utilizing a visible commercial LED, demonstrates strong room temperature orange down-converted emission. The exclusive adoption of the 'near' regular octahedral structure of the Te(IV)-halide unit provides a unique opportunity to unravel the role played by the $5s^2$ lone pair induced distortion in shaping its luminescence properties. Further synthetic efforts on developing strongly emissive $[TeX_6]^{2-}$ hybrids utilizing a common templating ligand are underway that would allow drawing a discernible structure/distortion-photophysical property correlation for the 'Pb-free' 0D (Te, Sb, Sn) hybrid luminescent materials.

Conflicts of interest

The authors declare no competing financial interest.

Acknowledgements

The authors acknowledge Milan K Bisai (NCL Pune), Dr J. Nithyanandhan (NCL Pune), and Dr R. Vaidhyanathan (IISER Pune), for insightful discussion. This work was financially supported by DST (Grant No. CRG/2019/000252). A. B. acknowledges CSIR for the Senior Research Fellowship.

References

1 C. C. Stoumpos and M. G. Kanatzidis, *Acc. Chem. Res.*, 2015, **48**, 2791–2802.
2 B. Saparov and D. B. Mitzi, *Chem. Rev.*, 2016, **116**, 4558–4596.
3 C. C. Stoumpos, C. D. Malliakas and M. G. Kanatzidis, *Inorg. Chem.*, 2013, **52**, 9019–9038.
4 S. D. Stranks, G. E. Eperon, G. Grancini, C. Menelaou, M. J. P. Alcocer, T. Leijtens, L. M. Herz, A. Petrozza and H. J. Snaith, *Science*, 2013, **342**, 341.
5 X. Hong, T. Ishihara and A. V. Nurmikko, *Phys. Rev. B: Condens. Matter Mater. Phys.*, 1992, **45**, 6961–6964.
6 Z.-P. Wang, J.-Y. Wang, J.-R. Li, M.-L. Feng, G.-D. Zou and X.-Y. Huang, *Chem. Commun.*, 2015, **51**, 3094–3097.
7 C. Zhou, H. Lin, Y. Tian, Z. Yuan, R. Clark, B. Chen, L. J. van de Burgt, J. C. Wang, Y. Zhou, K. Hanson, Q. J. Meisner, J. Neu, T. Besara, T. Siegrist, E. Lambers, P. Djurovich and B. Ma, *Chem. Sci.*, 2018, **9**, 586–593.
8 B. M. Benin, D. N. Dirin, V. Morad, M. Wörle, S. Yakunin, G. Rainò, O. Nazarenko, M. Fischer, I. Infante and M. V. Kovalenko, *Angew. Chem., Int. Ed.*, 2018, **57**, 11329–11333.
9 R. T. Williams and K. S. Song, *J. Phys. Chem. Solids*, 1990, **51**, 679–716.
10 K. M. McCall, C. C. Stoumpos, S. S. Kostina, M. G. Kanatzidis and B. W. Wessels, *Chem. Mater.*, 2017, **29**, 4129–4145.
11 M. D. Smith, A. Jaffe, E. R. Dohner, A. M. Lindenberg and H. I. Karunadasa, *Chem. Sci.*, 2017, **8**, 4497–4504.
12 R. S. Knox, Introduction to Exciton Physics, in *Collective Excitations in Solids*, Springer, Boston, 1983.
13 A. Vogler and H. Nikol, *Comments Inorg. Chem.*, 1993, **14**, 245–261.
14 K. M. McCall, V. Morad, B. M. Benin and M. V. Kovalenko, *ACS Mater. Lett.*, 2020, **2**, 1218–1232.
15 M. D. Smith and H. I. Karunadasa, *Acc. Chem. Res.*, 2018, **51**, 619–627.
16 Z. Xiao, Z. Song and Y. Yan, *Adv. Mater.*, 2019, **31**, 1803792.
17 C. Zhou, M. Worku, J. Neu, H. Lin, Y. Tian, S. Lee, Y. Zhou, D. Han, S. Chen, A. Hao, P. I. Djurovich, T. Siegrist, M.-H. Du and B. Ma, *Chem. Mater.*, 2018, **30**, 2374–2378.
18 Z. Li, Y. Li, P. Liang, T. Zhou, L. Wang and R.-J. Xie, *Chem. Mater.*, 2019, **31**, 9363–9371.
19 D. Chen, F. Dai, S. Hao, G. Zhou, Q. Liu, C. Wolverton, J. Zhao and Z. Xia, *J. Mater. Chem. C*, 2020, **8** 7322–7329.
20 F. Lin, H. Wang, W. Liu and J. Li, *J. Mater. Chem. C*, 2020, **8**, 7300–7303.
21 V. Morad, S. Yakunin and M. V. Kovalenko, *ACS Mater. Lett.*, 2020, **2**, 845–852.
22 A. Biswas, R. Bakthavatsalam, B. P. Mali, V. Bahadur, C. Biswas, S. S. K. Raavi, R. G. Gonnade and J. Kundu, *J. Mater. Chem. C*, 2021, **9**, 348–358.
23 D. Liu, Q. Li, Z. Zhang and K. Wu, *New J. Chem.*, 2019, **43**, 14892–14897.
24 B. Krebs and F.-P. Ahlers, *Adv. Inorg. Chem.*, 1990, **35**, 235–317.
25 T. V. Sedakova, A. G. Mirochnik and V. E. Karasev, *Opt. Spectrosc.*, 2011, **110**, 755–761.
26 T. V. Sedakova and A. G. mMirochnik, *Opt. Spectrosc.*, 2015, **119**, 54–58.
27 A. E. Maughan, A. M. Ganose, D. O. Scanlon and R. J. Neilson, *Chem. Mater.*, 2019, **31**, 1184–1195.
28 N. Kuhn, A. Abu-Rayyan, K. Eichele, C. Piludu and M. Steimann, *Z. Anorg. Allg. Chem.*, 2004, **630**, 495–497.
29 M. H. Ben Ghozlen and J. W. Bats, *Acta Crystallogr., Sect. B: Struct. Crystallogr. Cryst. Chem.*, 1982, **38**, 1308–1309.
30 W. Abriel, *Acta Crystallogr., Sect. B: Struct. Sci.*, 1986, **42**, 449–453.
31 A. Waśkowska and J. J. Z. Czapla, *J. Alloys Compd.*, 1993, **196**, 255–257.
32 I. Caracelli, *Z. Kristallogr. - New Cryst. Struct.*, 2004, **219**, 273–274.
33 N.-N. Shen, M.-L. Cai, Y. Song, Z.-P. Ze-Ping Wang, F.-Q. Huang, J.-R. Li and X.-Y. Huang, *Inorg. Chem.*, 2018, **57**, 5282–5291.
34 G. Blasse, G. J. Dirksen and W. Abriel, *Chem. Phys. Lett.*, 1987, **136**, 460–464.

35 S. S. Yakunin, B. M. Benin, Y. Shynkarenko, O. Nazarenko, M. I. Bodnarchuk, D. N. Dirin, C. Hofer, S. Cattaneo and M. V. Kovalenko, *Nat. Mater.*, 2019, **18**, 846–852.
36 B. M. Benin, K. M. McCall, M. Worle, V. Morad, M. Aebli, S. Yakunin, Y. Shynkarenko and M. V. Kovalenko, *Angew. Chem., Int. Ed.*, 2020, **59**, 14490–14497.
37 A. K. Viswanath, J. I. Lee, D. Kim, C. R. Lee and J. Y. Leem, *Phys. Rev. B: Condens. Matter Mater. Phys.*, 1998, **58**, 16333.
38 G. A. Ozin and A. V. Voet, *Can. J. Chem.*, 1971, **49**, 704–708.
39 D. J. Stufkens, *Recl. Trav. Chim. Pays-Bas*, 1970, **89**, 1185–1201.